

DIGITAL AND ROBOTIC TWINNING FOR VALIDATION OF PROXIMITY OPERATIONS AND FORMATION FLYING

Aviad Golan^{*†}, Gregory Zin^{*†}, Zahra Ahmed[‡], Emily Bates[‡], Toby Bell[‡], Pol Francesch Huc[‡], Samuel Y. W. Low[‡], Juergen Bosse[§], Simone D’Amico[¶]

In spacecraft Rendezvous, Proximity Operations (RPO), and Formation Flying (FF), the Guidance Navigation and Control (GNC) system is safety-critical and must meet strict performance requirements. However, validating such systems is challenging due to the complexity of the space environment, necessitating a verification and validation (V&V) process that bridges simulation and real-world behavior. The key contribution of this paper is a unified, end-to-end digital and robotic twinning framework that enables software- and hardware-in-the-loop testing for multi-modal GNC systems. The robotic twin includes three testbeds at Stanford’s Space Rendezvous Laboratory (SLAB): the GNSS and Radiofrequency Autonomous Navigation Testbed for Distributed Space Systems (GRAND) to validate RF-based navigation techniques, and the Testbed for Rendezvous and Optical Navigation (TRON) and Optical Stimulator (OS) to validate vision-based methods. The test article for this work is an integrated multi-modal GNC software stack for RPO and FF developed at SLAB. This paper introduces the hybrid framework and summarizes calibration and error characterization for the robotic twin. Then, the GNC stack’s performance and robustness is characterized using the integrated digital and robotic twinning pipeline for a full-range RPO mission scenario in Low-Earth Orbit (LEO). The results shown in the paper demonstrate consistency between digital and robotic twins, validating the hybrid twinning pipeline as a reliable framework for realistic assessment and verification of GNC systems.

INTRODUCTION

Autonomous Guidance, Navigation, and Control (GNC) is a key enabler for capabilities related to Rendezvous, Proximity Operations (RPO) and Formation Flying (FF) with Distributed Space Systems (DSS). Due to the inherent cost and inaccessibility of testing GNC software in space, validation with digital and robotic twins is often adopted as best practice. Digital twins are virtual models of the spacecraft that are necessary for rapid prototyping and faster-than-realtime numerical simulations. The process of using a digital twin to validate an algorithm is referred to as Software-in-the-Loop (SIL) testing. While SIL is a critical step in the GNC validation process, digital twins cannot fully capture the complexity and imperfections of flight hardware operating in the actual space environment. This is referred to as the “sim-to-real” gap. Instead, robotic twins that integrate true spacecraft hardware can be used to both verify the accuracy of the digital twin as well as evaluate algorithm robustness under real-world conditions. This is referred to as Hardware-in-the-Loop (HIL) testing.

^{*}The first two authors contributed equally to the paper.

[†]MS Candidate, Stanford University, Department of Aeronautics and Astronautics, Stanford, CA 94305.

[‡]PhD Candidate, Stanford University, Department of Aeronautics and Astronautics, Stanford, CA 94305.

[§]Managing Director, Robo-Technology GmbH, Benzstrasse 12, D-82178 Puchheim, Germany.

[¶]Associate Professor, Stanford University, Department of Aeronautics and Astronautics, Stanford, CA 94305.

Although SIL and HIL testing are common practice in the space domain, existing frameworks are often limited in their scope and their ability to test multiple GNC modalities across a full mission profile. Many testbeds lack the flexibility, scalability, and end-to-end capability needed to fully validate multi-modal GNC systems. In order to achieve the increasing level of autonomy and complexity required by future RPO and FF missions, it is necessary to develop more versatile, modular, and well-integrated approaches to GNC verification and validation (V&V).

To this end, this work implements a comprehensive, hybrid software- and hardware-in-the-loop framework for closed-loop testing of spacecraft GNC software using digital and robotic twinning. The digital twin architecture includes vision- and radiofrequency (RF)-based sensor models as well as models of the spacecraft actuators, which interface with high fidelity dynamics to simulate component behavior in the space environment. The robotic twin architecture incorporates three complementary testbeds at Stanford’s Space Rendezvous Laboratory (SLAB): the Testbed for Rendezvous and Optical Navigation (TRON)^{1,2} and Optical Stimulator (OS)^{3,4} for vision-based methods, the GNSS and Radiofrequency Autonomous Navigation Testbed for DSS (GRAND)⁵ for RF-based navigation techniques. Each hardware-based robotic twin may seamlessly replace components of the digital twin, enabling both rapid software prototyping and rigorous validation through hardware-based testing without significant additional overhead. The resulting framework can be integrated with a GNC software stack that enables flexible switching between GNC modes, including sensor types, navigation algorithms, control solvers, and guidance goals. This novel approach supports end-to-end testing for multi-modal GNC stacks across complete mission scenarios. This work presents experimental results showcasing the multimodal capabilities of this testing framework by evaluating the GNC stack’s performance across a representative mission scenario, including transitions between navigation and control modes and validation using both digital and robotic twins of sensors.

The remainder of the paper proceeds as follows. First, the “Survey of Existing Digital and Robotic Twins” section summarizes the state-of-the-art in digital and robotic twinning for DSS. Then, the “Hybrid Digital and Robotic Twinning Approach” section presents the novel framework used in this work and describes the capabilities, calibration procedures, and resultant accuracy of the individual robotic twins. The “Autonomous GNC Stack for RPO” and “Experiments” sections introduce the multi-modal GNC stack and representative mission trajectory that are used to test the digital and robotic twinning framework. Finally, the “Results” section details the SIL and HIL results and how they complement each other to provide more robust validation.

SURVEY OF EXISTING DIGITAL AND ROBOTIC TWINS

Digital Twin State-of-the-Art

It is common for different groups to develop proprietary software tools that are validated through rigorous mathematical derivation, flight heritage, or benchmarking against commercial platforms such as AGI’s Systems Tool Kit (STK). These tools are often highly specialized for specific applications, limiting their modularity or broader applicability. In contrast, state-of-the-art mission planning tools such GMAT⁶ and A.I Solutions’ FreeFlyerTM offer more generalized simulations environments. Similarly, programmable open-source modeling tools such as Basilisk⁷ and MATLAB / Simulink⁸ provide flexible platforms for spacecraft GNC V&V. Basilisk, in particular, includes interfaces for comparing simulations with real-time hardware-in-the-loop results, making it well-suited for integrated testing.⁹ However, Basilisk does not currently model camera physics in its image rendering which is essential for vision-based navigation techniques used in RPO. To support

robust flight software development, it is also critical to enable an iterative workflow, such as that offered by MATLAB/Simulink, while frequently testing against real-world hardware. This ensures resilience to practical imperfections such as limited memory, intermediate process scheduling, and unmodeled noise. With those key features in mind, a custom novel event-driven simulation environment was developed by SLAB.¹⁰ It was originally created to support GNC flight software validation for the VISORS mission¹¹ and later extended to support the RPO stack developed by SLAB.¹²

Robotic Twin State-of-the-Art

It is inherently challenging to design a digital twin that substitutes well for physical testing until realistic operational conditions. Augmenting SIL tests with HIL ensures comprehensive end-to-end system validation of the test article. HIL testbeds serve as physical stand-ins for capabilities that are difficult to model or simulate accurately, helping validate both the algorithm and the digital twin itself. There are several types of HIL testbeds, including GNSS signal simulators, optical stimulators, kinematic spacecraft simulators, and dynamic spacecraft simulators.¹³

GNSS Simulators: GNSS HIL simulators serve a crucial role enabling high-fidelity and real-time validation of navigation flight software. NASA Goddard Space Flight Center has developed a modular Formation Flying Test Bed (FFTB) since 2001 which eventually supported notable missions such as GRACE and MMS.¹⁴ The FFTB was extended to integrated closed-loop end-to-end GNC¹⁵ in 2004. The German Space Operations Center (GSOC) and DLR too had developed their own native FFTB using a mission-independent Simulink-based architecture, to support rapid GNSS software prototyping.^{16,17} Commercial options such as the Spirent GSS8000¹⁸ and IFEN NCS¹⁹ have become popular options for integration into existing test beds since the past two decades as well. Commercial products have supported development in multiple applications of spaceborne GNSS, such as (1) a precise orbit determination testbed for single spacecraft²⁰ at the University of New South Wales, (2) a testbed for ionospheric remote sensing using multi-constellation receivers in space²¹ at Virginia Tech, and (3) a high-precision relative navigation testbed in support of a diverse portfolio of FF/RPO missions^{5,22} at the Stanford Space Rendezvous Lab.

Optical Stimulators: Optical stimulators are test benches designed for component-level validation of vision-based sensors such as star trackers. These testbeds use collimated light sources to simulate distant objects, such as stars or spacecraft, on a digital screen. The rendered imagery is then used to stimulate the vision-based sensor under test. Examples of optical stimulators include the John Hopkins University Applied Physics Laboratory's Celestial Object Simulator (CEL),²³ DLR's Jenoptik Optical Sky field Simulator (OSI),²⁴ Technical University of Denmark's Optical Stimulator System for VBS (OSVBS),²⁵ and the University of Naples' testbed.²⁶ While optical stimulators are compact, simple, and enable testing of GNC using real hardware, the spacecraft motion is still simulated in software only. Additionally, they are limited in ability to account for narrower or wider field of views (FOV) when testing different vision-based sensors. Finally, they are often unable to simulate close-range scenarios when light from an object is no longer collimated.⁴

Kinematic Testbeds: In contrast, kinematic testbeds physically model spacecraft motion to emulate commanded positions and orientations using high-torque actuators that are not representative of the true spacecraft actuators. They are primarily used for validating sensor performance and navigation algorithms, offering a modular and reconfigurable platform for testing vision-based GNC systems. Examples of existing kinematic testbeds include DLR's European Proximity Operation Simulator (EPOS)^{27,28} and EPOS 2.0,²⁹ Lockheed Martin's Spacecraft Operations Simulation Center (SOSC),³⁰ DLR's Testbed for Robotic Optical Navigation (TRON),³¹ and NASA Marshall

Space Flight Center’s Dynamic Overhead Target Simulator (DOTS).³² These testbeds include varying number of degrees-of-freedom (DOF), lighting conditions, and number of test articles. However, kinematic testbeds do not model true spacecraft dynamics, and are physically constrained by the size of the test facility, which often limits them to testing close-range GNC algorithms.

Dynamics Testbeds: Dynamic testbeds instead do model the true spacecraft dynamics by using realistic actuation and a facility designed to minimize dynamic interaction between the test article and the local environment, thereby simulating spacecraft dynamics. A common way to do this is through the use of air-bearing tables, which create a frictionless surface using a thin film of pressurized gas that allows the spacecraft to simulate 3-DOF motion (2 translational and 1 rotational DOF). Examples include the Naval Postgraduate School’s Proximity Operations of Spacecraft: Experimental hardware-In-the-loop DYNAMIC simulator (POSEIDYN),³³ NASA JPL’s Small Satellite Dynamics Testbed (SSDT),^{34,35} Naval Postgraduate School’s Three-Axis Simulator (TAS-2),³⁶ and Stanford University’s Free Flyer Testbed.³⁷ Additional facilities combine multiple platforms using flat air-bearing tables and spherical-bearing tables to achieve 5 or 6 DOF, such as Georgia Institute of Technology’s Autonomous Spacecraft Testing of Robotic Operations in Space (ASTROS) testbed.³⁸ Finally, other testbeds use a combination of kinematic and dynamic approaches to achieve full 6-DOF motion, such as California Institute of Technology’s Multi-Spacecraft Testbed for Autonomy Research (M-STAR).³⁹ While dynamic testbeds confer better fidelity in spacecraft dynamics, they are less modular and more operationally complex. They require fully self-contained test articles with onboard power, actuation, and computation, making them more resource-intensive to develop and operate. Similar to kinematic testbeds, dynamic testbeds are similarly limited by the size of the facility and thus cannot be used for testing far-range GNC capabilities.

Each type of HIL testbed offers key validation capabilities over pure SIL testing and serves a distinct role in the GNC validation pipeline. However, they also introduce practical constraints such as the type of GNC modes they can support (e.g. vision-based versus RF-based navigation), the inter-satellite distances they can replicate, and the fidelity of spacecraft dynamics they can achieve. Thus, no testbed alone can support multi-model GNC V&V across a full-range trajectory.

HYBRID DIGITAL AND ROBOTIC TWINNING APPROACH

To overcome the limitations of existing testbeds and tools, this work introduces a hybrid digital and robotic twinning approach for spacecraft GNC validation. The digital twin models high-fidelity spacecraft sensors and actuators entirely in software, enabling rapid and repeatable simulations. Its sensor models consist of an OpenGL-based renderer coupled with a camera model and a target spacecraft CAD model to simulate optical measurements and a GNSS Emulator for RF-based measurements. For the purposes of this work, ideal actuators are modeled without any dynamics, as impulsive Δv is directly applied to the system. In total, this digital twin enables testing of far-, mid-, and near-range vision-based and radio-frequency (RF) based navigation algorithms in closed-loop with control. The robotic twins are hardware components that can seamlessly replace one or more of the simulated sensors for hardware-in-the-loop testing. More specifically, the robotic twins consist of three distinct testbeds: the Optical Stimulator (OS),^{3,4} the Testbed for Rendezvous and Optical Navigation (TRON),^{1,2} and the GNSS and Radiofrequency Autonomous Navigation Testbed for Distributed Space Systems (GRAND).⁵ The OS is used to test far-, mid-, and close-range vision-based navigation algorithms using star-trackers and monocular cameras coupled with synthetically rendered space scenes. TRON is instead used for testing close-range navigation algorithms using an optical payload, a scaled model of the target, and realistic illumination conditions

Table 1: High-level overview of the digital and robotic twin used in the hybrid framework.

| Robotic Twin | ISD Range | Sensing Mode | Hardware Components | Digital Twin Analog |
|---------------------|---------------------|---------------------|---|----------------------------|
| OS | Far Mid Close | Vision | Optical Payload | OpenGL-Based Renderer |
| TRON | Close | Vision | Optical Payload Spacecraft Model Albedo Light boxes | OpenGL-Based Renderer |
| GRAND | Far Mid Close | RF | GNSS Signal Simulator GNSS Receiver | GNSS Emulator |

to create pseudo-spaceborne imagery. Finally, GRAND enables testing of RF-based navigation in far-, mid-, and close-range scenarios using a multi-GNSS signal generator coupled with numerical simulation of ground truth dynamics. The integration of these three testbeds enables coverage of multi-modal GNC HIL validation across far-, mid-, and close-range distances. Table 1 summarizes the robotic twin testbed capabilities in terms of applicable Inter-Satellite Distances (ISD), sensing modes, hardware components, and which digital twin modules they replace.

Figure 1 provides an overview of the hybrid framework and how the digital and robotic twins can be interchanged to test an autonomous GNC software stack. First, given a set of initial conditions, any SIL or HIL test is driven by a single source of ground truth dynamics. The ground truth dynamics are fed into either the digital twin’s sensor models or the corresponding robotic twin testbed, which ultimately output measurements that are used as inputs for GNC. The GNC stack is either executed on a host computer to isolate the algorithm performance or can alternatively be embedded onto an on-board computer (OBC) to additionally account for the compute constraints of flight hardware. The GNC stack responds with control inputs as necessary, which are carried out by the digital twin’s actuator models, thus updating the ground truth state.

Overall, the hybrid framework offers two key benefits: modularity and versatility. Its modular structure allows for incremental testing of the GNC stack’s sensitivity to various sources of error, such as sensor imperfections or environment uncertainties, by gradually introducing physical components. For example, a test can begin using only the digital twin models, then incorporate the OS to assess the impact of using a physical optical payload, and finally transition to TRON to understand the combined impact of real hardware and realistic illumination. In terms of versatility, this approach can support a broad range of mission and sensor types, including combinations of sensors and transitions between modalities. The flexibility of this approach makes it well-suited for early-stage algorithm development as well as later-stage hardware-in-the-loop validation.

High-Fidelity Spacecraft Dynamics

In this framework, the ground truth orbit dynamics are propagated using SLAB’s high-fidelity astrodynamics library, S^3 .⁵ The simulation integrates Gauss Variational Equations (GVE) using the Dormand–Prince method⁴⁰ with an adaptive step size to bound truncation error. The modeled perturbations include a 60x60 GGM05S spherical harmonic gravity model, the NRLMSISE-00 atmospheric model⁴¹ with a cannonball drag model, and solar radiation pressure (SRP) with a cylin-

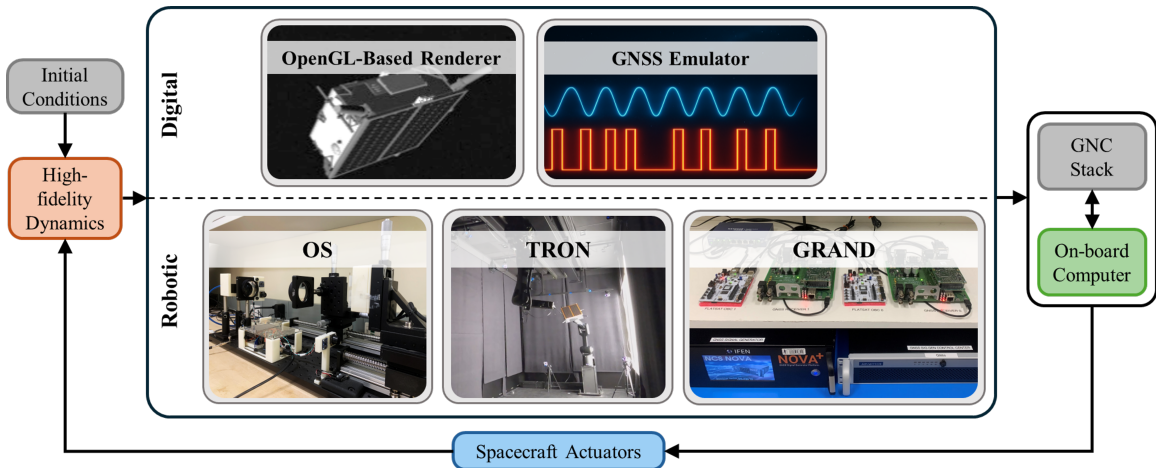


Figure 1: Digital and robotic twinning framework. Reference truth is simulated on a host computer with optional sensor models, supporting either a digital twin (top) or robotic testbed (bottom). The GNC stack may execute either on the host or flight computer, with actuators modeled in software.

drical Earth shadow. Currently, the ground truth propagation additionally includes perturbation-free attitude dynamics in order to simulate a tumbling target spacecraft. Extending the fidelity of the attitude propagation is left for future work.

Digital Twin

The backbone of the digital twin is an event-driven simulation environment written in C++ adopting the high-fidelity dynamics described in section “High-Fidelity Spacecraft Dynamics”. It supports the queuing and execution of events, maneuvers, measurements, telemetry, and telecommands, with realistic latencies.¹⁰ It includes a rich library of synthetic emulators for measurements and actuation models, designed for rapid, iterative development of GNC stacks for distributed space systems. It combines a high-fidelity OpenGL-based renderer for synthetic image generation in vision-based navigation, together with software-emulated GNSS measurements and broadcast ephemeris for RF-based navigation. The synthetic images are generated in OpenGL using SLAB’s Optical Stimulator software⁴ given a spacecraft CAD model and camera model. The renderer has been upgraded to include realistic semi-resolved imagery in addition to non-resolved point sources and fully resolved objects. It includes an accurate star field and configurable illumination conditions with both specular and diffuse reflections.

The GNSS Emulator provides a faster-than-realtime alternative to the HIL GRAND testbed, by augmenting the event-driven simulation environment¹⁰ with a GPS constellation of 31 space vehicles emulating pseudorange and carrier phase measurements packaged into NovAtel-format binaries,⁴² corrupted with ionospheric effects on the group delay and phase advance, carrier phase ambiguities, clock errors, thermal noise and body frame offsets due to the Center-of-Mass (COM) to Phase Center Offset (PCO), as tabulated in Table 2 and Table 3.

The SIL emulated crosslink, for mutual exchange of GNSS measurements between cooperative spacecraft, models stochastic transmission delay, with message delivery failure. This can expose weaknesses resulting from non-robust navigation algorithms with a reliance on shared measurements, common in Carrier Phase Differential GNSS (CDGNSS). This environment supports deter-

Table 2: GNSS signal-in-space modeling⁴³

| | |
|-------------------------------|----------------------------|
| GNSS signals | GPS L1 only, Block IIR-M |
| GNSS aperture | 170 degrees |
| GNSS gain pattern | Spherical only |
| GNSS ephemeris source | Broadcast (no corrections) |
| Ionospheric model | Klobuchar (delay) |
| Earth horizon mask | -20° from horizon |
| Receiver aperture mask | 190 degrees |
| Receiver simulated LNA | 33 dBW |
| Receiver gain pattern | ANTCOM 1.9G1215A |
| Thermal noise model | Psiaki et al ⁴⁴ |

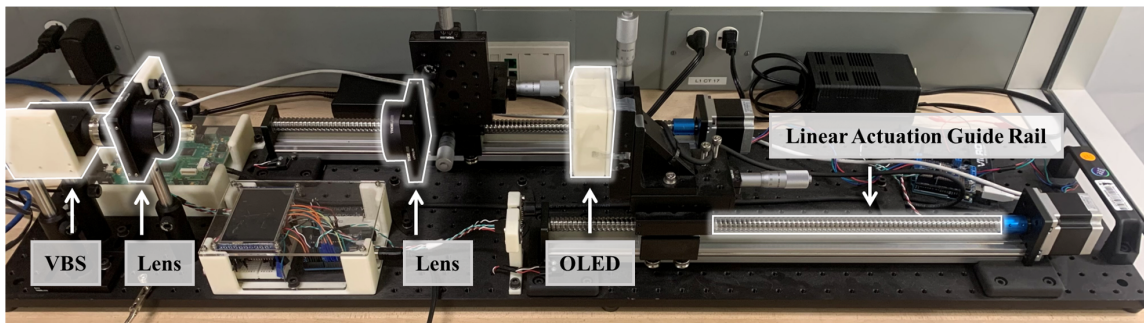
Table 3: Spacecraft uncertainty parameters⁴³

| Parameter | Unit | Dist. | Value |
|-------------------------------|--------|----------|-------|
| Spacecraft mass | kg | Gaussian | 0.04 |
| Spacecraft COM | mm | Uniform | 3 |
| GNSS antenna PCO bias | mm | - | 50 |
| GNSS antenna PCO noise | mm | Gaussian | 1 |
| GNSS antenna direction | arcsec | Gaussian | 30 |
| Attitude knowledge | arcsec | Gaussian | 20 |
| Maneuver errors | - | Ideal | - |

ministic, faster-than-real-time execution, enabling developers to simulate multi-spacecraft missions, debug complex interactions, and identify implementation-level defects, e.g., memory exhaustion or communication faults which are capabilities not found in traditional HIL setups.¹⁰

Optical Stimulator (OS)

The OS is a variable-magnification optical bench designed to stimulate a wide range of vision-based sensors using synthetically generated space scenes. The advantage of the OS is that it replaces the camera model used in the digital twin with real hardware to capture sensor noise and distortion that are difficult to model accurately. The testbed consists of a vision-based system (VBS) test article, two corrective lenses, and an organic light-emitting diode (OLED) microdisplay as shown in Figure 2. The lenses and OLED monitor can be moved along a rail using motorized lead screws to vary the magnification of the scene depending on the VBS FOV. In this work, the VBS used is a PointGrey GrassHopper3-PGE-23S6M-C with a Xenoplan 1.935 mm lens, and a FOV of 18.3°. However, the platform allows users to use whatever camera is best suited to the relevant mission, such as a star tracker. The OS renders a space environment scene using the same OpenGL-based renderer described in the Digital Twin section. The OLED display and camera are operated by a MATLAB program running on a host computer. During HIL testing, the simulation calls the MATLAB OS control program at the prescribed imaging rate, triggering the camera to take an image which is returned via Ethernet. The simulator supports various imaging rates by pausing the simulation until an image is returned to the GNC stack.

**Figure 2:** Optical Stimulator testbed. Ref. 45.

Ref. 45 details the OS calibration process, which is designed to ensure geometric and radiometric accuracy. The geometric calibration process removes the corrective lens distortion and tunes how

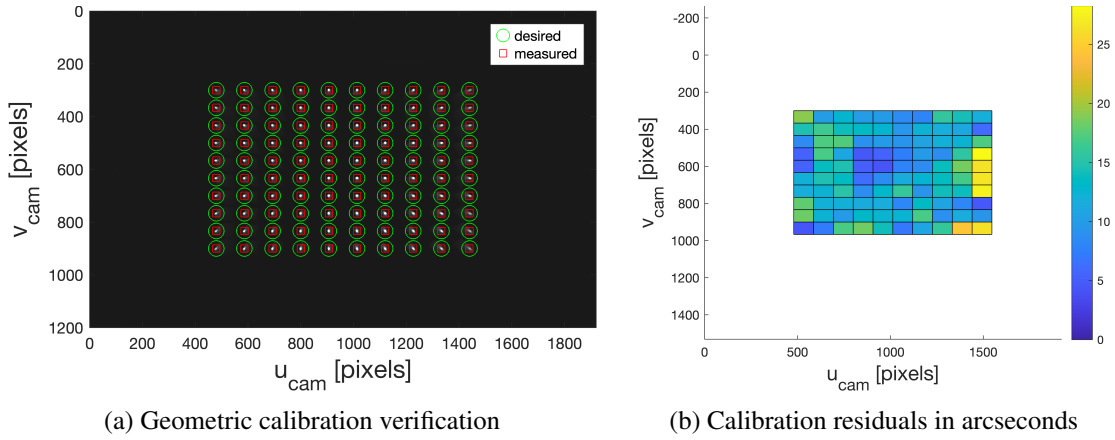


Figure 3: Optical Stimulator calibration results

the synthetic scene is rendered on the OLED monitor. The radiometric calibration characterizes the irradiance contribution from a single OLED pixel. Together, these steps ensure that light will reach the VBS aperture from the desired angular location with the correct visual magnitude. To validate the distortion calibration parameters, a set of known unit vectors are used to display a grid of dots on the OLED monitor after their directions are warped using the optimal distortion coefficients introduced by the corrective lenses. When the VBS captures an image, the measured grid locations should result in the known, given unit vectors again. Calibration with the PointGrey 35 mm lens produces residuals with mean 12.5 arcsec and standard deviation 5.1 arcsec. A visual of the calibration residuals shown in Fig. 3 includes a heatmap of the residuals in pixel space.

Testbed for Rendezvous and Optical Navigation (TRON)

TRON is a multi-purpose robotic testbed for verification and testing of vision-based navigation at close-range. TRON features two KUKA industrial robots, simulating kinematic motion of a chaser spacecraft and a target object. The robots can achieve precise positions with 0.03 mm motion repeatability. The first robot is a 7-degree-of-freedom (7-DOF) robotic manipulator that travels along a 7 m ceiling-mounted track. A space-capable Point Grey Grasshopper 3 camera with a Xenoplan 1.4/17 mm lens is mounted on the end-effector to observe a target spacecraft or planetary body. Like the OS, this camera can be replaced in scenarios where a particular camera is to be tested. The second robot is a 6-DOF grounded robotic arm, equipped with a mount which allows the attachment of a mockup model of the target object. Each robot reports internal joint angles; through forward kinematics, the position and orientation of its end effector is known with respect to a origin defined in the KUKA reference system. The TRON facility also includes a sun lamp and 10 wall-mounted Earth albedo lightboxes which are controlled together to accurately simulate the illumination conditions of space. All surfaces are painted with a radiation-absorbing paint to mitigate unwanted reflections.

The TRON facility also features 12 Vicon motion capture cameras, which are mounted on ceiling rafters and tripods to provide full coverage of the facility. The Vicon cameras track reflective spheres that are rigidly attached to the target and camera and reports their positions and orientations with respect to a local reference frame. To establish the transformation between the Vicon reference frame and the global KUKA frame, five fixed Vicon monuments equipped with 14 mm reflective

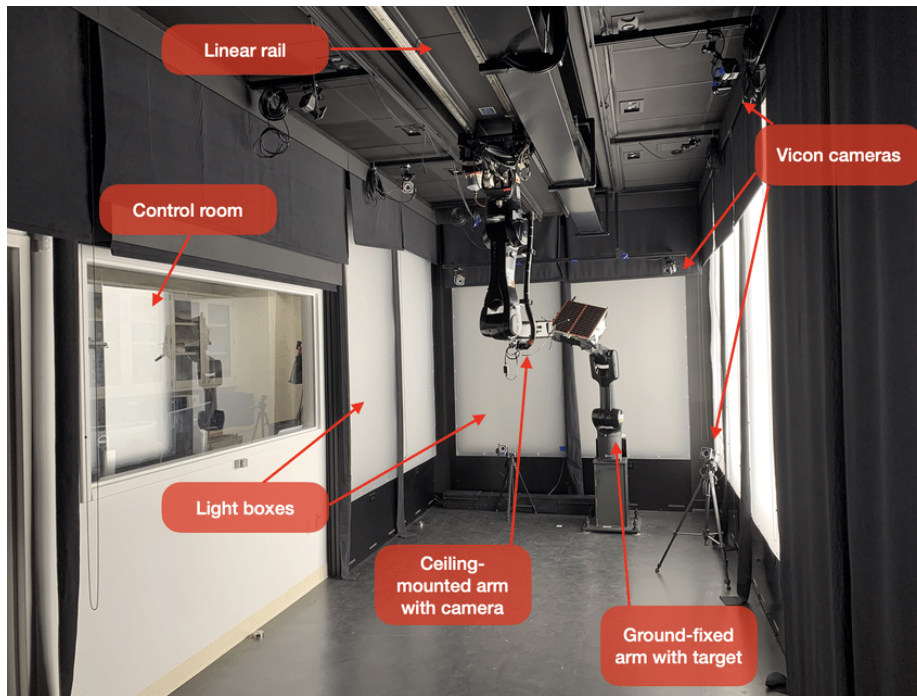


Figure 4: TRON Facility. Figure from Ref. 2.

spheres are strategically placed throughout the facility. The true positions of these monuments were accurately measured using a Leica AT403 laser tracker⁴⁶ yielding ground-truth spatial coordinates within an accuracy of $U(x, y, z) = 15 \mu\text{m} \pm 6 \mu\text{m}/\text{m}$ and serve as the origin for the Kuka reference frame. With the added reflective spheres, the Vicon system can detect the monuments and align its local frame to the Kuka reference frame. The Vicon system provides secondary measurements that are independent from the robots, which increases TRON’s calibration accuracy.

Like the OS, the TRON system is operated through a MATLAB function, which is invoked by the simulation during closed-loop operation. The function receives a relative pose and lighting direction as inputs, and returns an image from the VBS for use by the GNC stack. Specifically, it computes the desired robot positions in joint-angle space along with lightbox settings based on the input pose and lighting direction vectors. The resulting joint angles are converted into a motion trajectory satisfying dynamic constraints and transmitted to the robot controllers via KUKA’s Robot Sensing Interface (RSI) over a 250 Hz UDP connection. The KUKA robot end-effector achieved positions are then reported back to the host computer via TCP/IP. Once the desired position is achieved, the function triggers the VBS to take an image, which is returned to the host computer via Ethernet. When the image is passed back to the GNC stack, a helper function applies a boolean mask to replace all background pixels not occupied by the target with a rendered star field.

The calibration process of TRON begins with an absolute calibration of the robots, where the robots’ joint offsets are estimated. The joint offsets—which lead to imprecise knowledge of the robots’ positions via forward kinematics—are caused by manufacturing tolerances, wear, or mechanical misalignment, so the absolute calibration is not often performed as the estimates maintain their validity for long periods. The process involves the collection of images by a camera attached to the ceiling mounted robot of a ChArUco board attached to the other robot. Images are taken

Table 4: Robot World Hand-Eye Calibration Results (Mean \pm Std)

| Metrics | KUKA-only RWHE | Vicon-only RWHE | Data Fusion |
|--------------------|-------------------|-------------------|-------------------|
| E_T [mm] | 7.345 ± 4.550 | 4.535 ± 2.938 | 4.171 ± 2.773 |
| E_R [$^\circ$] | 0.482 ± 0.440 | 0.376 ± 0.448 | 0.399 ± 0.443 |
| E_p [pix] | 8.123 ± 5.462 | 4.571 ± 2.993 | 3.810 ± 2.253 |

to maximize the diversity of relative poses achieved, even if these poses would not be experienced during regular operations. The relative pose information from the robots, Vicon, and via solving the PnP for the ChArUco board is used to estimate the robot joint offsets via nonlinear least-squares. A correction to the joint offsets is then calculated and applied to the robot commands leading to more precise positioning.

The second calibration step for TRON involves estimating the relative position and orientation between the robot end effectors and the mounted objects—camera or target. Ref 2 provides details on this calibration process, which uses the same measurement sources as before and performs Bayesian data fusion to increase the accuracy of the estimated offsets.

The calibration results of this work are shown in Table 4. Note that the results reported here have slightly lower accuracy compared to previously published results with this same method. This is due to a larger coverage of states, spanning all feasible positions within the TRON facility, whereas previous calibrations were done in a limited region of the facility.

GNSS and Radiofrequency Autonomous Navigation Testbed for DSS (GRAND)

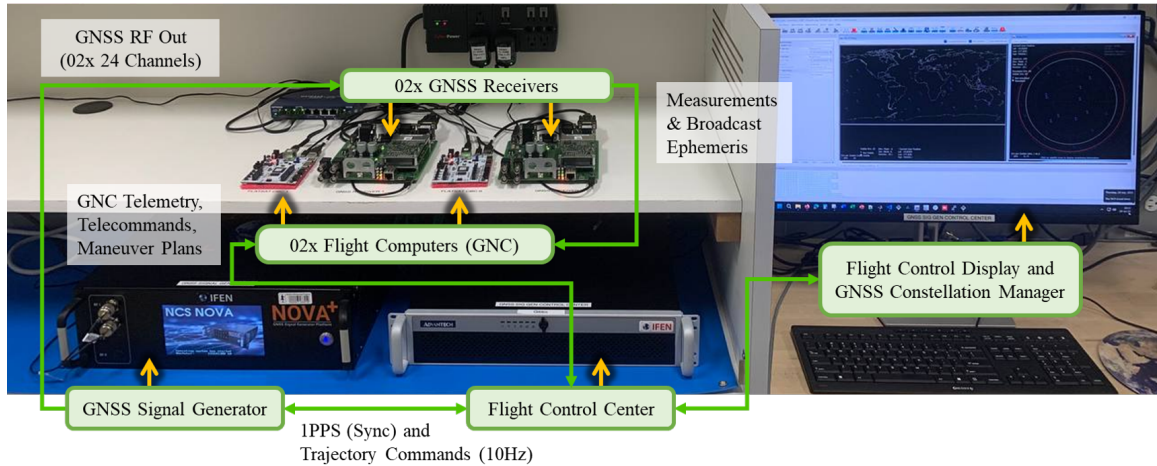


Figure 5: The GRAND testbed, comprising (i) an IFEN NOVA+ 2020 multi-GNSS signal generator, (ii) the ground flight control center, and (iii) a set of NovAtel OEM628 GNSS receivers, with flight heritage, connected serially to ZYNQ7000 SoC boards equivalent to the VISORS flight computers. Both GNSS receiver and flight computer models possess flight heritage. The ZYNQ7000 flight computers can be used to host C-compatible GNC software test articles.

The GRAND testbed of Figure 5 enables real-time evaluation of flight software and its navigation algorithms where GNSS is concerned. GRAND was originally conceived to test the Distributed

multi-GNSS Timing and Localization (DiGiTaL) software package, to achieve precise relative navigation between cooperative spacecraft using CDGNSS with Integer Ambiguity Resolution (IAR).⁴⁷ It has since been upgraded from its original design⁵ in three critical ways. First, the original IFEN NavX has been upgraded to an IFEN NOVA+, with greater channel bank support, and with hardware compatibility with future and modern multi-GNSS signals such as Galileo E6B and BeiDou B2b. Second, the Flight Control Center has a much more powerful and modern Intel Core i7-14700K (3.40 GHz) processor, in order to support the simulation of more sophisticated ground-based tasks while running the event-driven simulation environment. Third, the GRAND testbed has been fully integrated with the event-driven simulation architecture aforementioned in the Digital Twin section.¹⁰ The Flight Control Center is synchronized with the IFEN NOVA+ via a 1PPS line. Ground truth dynamics are fed to the IFEN NOVA+ over a UDP socket at 10 Hz, which provides a flight trajectory that is interpolated for fine-sampling. The IFEN NOVA+ produces RF GNSS signals from a simulated GNSS constellation, where the measurements are such that they emulate receivers that are consistent with an input flight trajectory. The GNSS receivers in turn provide measurements and ephemeris to the payload GNC software, which can optionally be hosted in the flight computers. Runtime analyses can then be conducted for the flight software within the embedded Linux environment of the flight computers, which run on an ARMv7 architecture. GRAND has successfully validated real-time execution of the VISORS GNC stack,¹¹ the RPO GNC stack,¹² and continues to serve as a critical testbed for the DiGiTaL software.^{43,48}

AUTONOMOUS GNC STACK FOR RPO

The autonomous GNC stack for RPO and FF used as the test article for this work is a software architecture that supports GNC operations across all mission phases, from initial acquisition to docking, using a unified framework deployed on one or more “chaser” spacecraft. The full details for this GNC stack are described in Ref. 12, and the high-level architecture and algorithms are summarized here.

The GNC architecture comprises four core modules: management, navigation, safety, and control. The management module handles operational mode transitions and fault detection, isolation, and recovery (FDIR). The navigation module fuses measurements from optional optical sensors, GNSS, and inter-satellite links to estimate relative and absolute states of targets using both batch initialization and sequential estimation. The safety module predicts potential collisions based on state estimates and provides risk metrics to the control system. The control module generates maneuver plans through a suite of solver algorithms, enabling autonomous trajectory planning, station keeping, and collision avoidance. The full architecture is shown in Figure 6, where external systems are shown in dark gray ovals and exchanged data is in blue. Internal subsystems are shown in light gray rectangles, navigation algorithms in green, and control in orange. Lastly, additional optional components are shown in dotted lines, and could be seamlessly integrated give the modular architecture of this GNC stack.

The architecture is designed to execute fully onboard, allowing servicers to autonomously navigate, manage system and safety constraints, and plan control actions in real time. A typical operational scenario involves transitioning between different sensing and control strategies, such as far-range angles-only tracking using star trackers and close-range pose estimation using fully-resolved imagery of a target spacecraft. The navigation module supports dynamic configurations, accommodating multiple agents and varying sensor data availability. Collision risk assessments, expressed in the servicer’s radial-tangential-normal (RTN) frame, inform maneuver planning to ensure safe

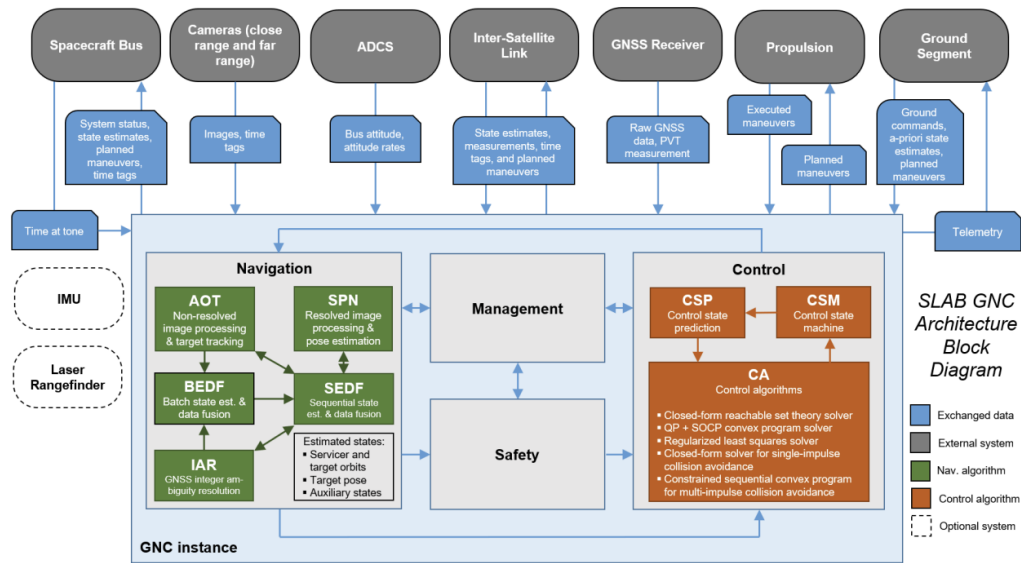


Figure 6: Autonomous GNC stack for RPO used as a test article in this paper. Figure from Ref.12

operation even under degraded conditions. Informed by the safety assessment and the estimated state, the control module uses an internal state machine to determine whether it is in a waypoint approach or station-keeping mode, then employs an appropriate control solver to achieve the control objective.

A subset of navigation, estimation, and control algorithms from this GNC stack are employed in the experiments that will be detailed in the next section. The high-level overview of the relevant algorithms is summarized in Tables 5 and 6.

EXPERIMENTS

To test a broad range of the modalities of the testing architecture and GNC stack, an RPO trajectory spanning from far to close range is proposed. The RPO trajectory consists of two spacecraft: a servicer spacecraft and a target. For this work, the target is the Tango spacecraft from the PRISMA mission.⁵⁸

RPO Trajectory

The servicer’s absolute orbit is a Sun-synchronous low-Earth orbit (LEO). Such an orbit is ideal for servicing missions due to consistent lighting conditions. The orbit is initialized with the quasi-nonsingular orbit elements listed in Table 7.

The reference trajectory consists of waypoints that parameterize the target’s relative orbit with respect to the servicer at certain points in time. The state representation is the set of six quasi-nonsingular relative orbital elements (ROEs) defined by D’Amico.⁵⁹ The complete waypoints of the mission are listed in Table 8, which includes an approach from far range (waypoints #0 to #8) to a close circumnavigation of the target for inspection (waypoints #9 to #12).

The target spacecraft begins at far range, approximately 75 kilometers behind the servicer in the along-track direction while approaching at a rate of 3.2 meters per second (waypoint #0). Then the

Table 5: Navigation and estimation algorithms tested in this work. Algorithms are a subset of the Autonomous GNC stack from Ref. 12. Table recreated from Ref. 12.

| Algorithm | Angles-Only Tracking (AOT) ⁴⁹ | Spacecraft Pose Network (SPN) ⁵⁰ | CDGNSS with IAR ^{43,51} | Sequential Estimation and Data Fusion (SEDF) ^{52,53} |
|--|--|---|---|---|
| Sensing Modality | Vision-based | Vision-based | RF-based | - |
| Relevant Techniques | Multi-hypothesis tracking Kinematic target modeling | Convolutional neural networks | mLAMBDA algorithm ^{47,54} | Unscented Kalman filter Adaptive process noise Statistical data association |
| Possible Inputs | Host camera images Host orbit estimate | Host camera images Host orbit estimate Host attitude estimate | Host GNSS Peer GNSS | Host & peer bearing angles Host & peer GNSS Host & peer camera attitude Host SPN heatmaps Host & peer state estimates Host & peer maneuver plan |
| Possible Outputs | Target bearing angles Sensor attitude | Target pose w.r.t. servicer | Resolved double-differenced integer ambiguities | Host absolute orbit estimate Peer relative orbit estimates Host absolute attitude estimate Peer relative attitude estimates Host & peer auxiliary state est. |
| Nominal Sample Time (LEO) | 60 sec | 10 sec | 10 sec | 5–120 sec |
| Representative Accuracy (1-σ) | <35" angle error <20" attitude error | <10 cm relative pos. <1° orientation | <1 cm relative position error | <5 m abs. pos. (GNSS w/out IAR) <5 cm rel. pos. (GNSS w/out IAR) <1 cm rel. pos. (GNSS with IAR) <1 km abs. pos. (angles-only) <2% $\delta\lambda$ rel. pos. (angles-only) <10 cm rel. pos. (SPN) <1° rel. att. (SPN) |
| Applicability | Non-resolved targets | Resolved targets w/ known 3D model | Cooperative targets | - |

rate of approach is reduced, and e/i vector separation is added to ensure passive safety (waypoints #1 to #3). The intersatellite distance is incrementally decreased from 1 kilometer to 50 meters (waypoints #4 to #8). At these waypoints, the target is semi-resolved when observed by the VBS systems used as test articles in this work.

Afterwards, the servicer begins a V-bar approach to an along-track separation of 8 meters (waypoint #9), where the target becomes fully resolved in the camera frame. At waypoint #10, the servicer transfers to a passively safe relative orbit with a radius of 3 meters, then switches to another relative orbit of the same radius (waypoint #11). The sequence of waypoint #10 and #11 establishes a close fly-by inspection orbit, allowing the servicer to collect data about the target from both sides of the orbit plane. Finally, the servicer will retreat to a distance of 8 meters and gradually drift away (waypoint #12).

Experiment Specifications

Table 9 summarizes the testing configuration for each experiment. Experiments are categorized as near-range or far-range depending on the inter-satellite distances associated with the trajectory waypoints used. With separations from tens to thousands of meters, waypoints 0-8 are considered far-range; with separations under 10 m, waypoints 9-12 are considered near-range. Experiments 1, 2, and 4 use an uncooperative target, meaning that it does not share navigation information with the servicer. In these experiments, the uncooperative target's attitude is not controlled. Conversely, Experiment 3 uses a cooperative target, meaning that it shares navigation information with the

Table 6: Controls algorithms tested in this work. Algorithms are a subset of the Autonomous GNC stack from Ref. 12. Table recreated from Ref. 12.

| Control Solver | Closed-Form ^{55,56} | Koenig-D'Amico SOCP/QP ⁵⁷ | Least Squares ¹¹ |
|---------------------------------------|---|---|---|
| Solution Type | Impulsive | Optimized impulsive | Time-fixed impulsive |
| Applicability | Large ISD Station-keeping Reconfiguration | Small ISD Trajectory Tracking | Small ISD Trajectory Tracking |
| Relevant Techniques | Reachable Set Theory | Reachable Set Theory Convex optimization | Least Squares with Tikhonov regularization |
| Maneuver Type | 3 T, 1-2 N | 4-6 RTN | 2-3 RTN |
| Maneuver Frequency | 0.5 Orbits | Optimized | Time-Fixed |
| Planning Horizon | >1.5 orbits | <1.5 orbits | <1.5 orbits |
| Control Loop Closure Frequency | 2 orbits | 60 sec | 60 sec |
| Nominal Accuracy | 1-10 m | 1-10 cm | 1-10 cm |

Table 7: Servicer Quasi-nonsingular Orbital Elements

| a [km] | e_x [-] | e_y [-] | i [°] | Ω [°] | u [°] |
|-----------|-----------|-----------|---------|--------------|---------|
| 7,087.297 | 0.0015 | 0.0 | 98.18 | 189.89 | 0.0 |

Table 8: End-to-end Mission ROE Waypoints

| Waypoint | Time (hr) | $a\delta a$ (m) | $a\delta\lambda$ (m) | $a\delta e_x$ (m) | $a\delta e_y$ (m) | $a\delta i_x$ (m) | $a\delta i_y$ (m) |
|----------|-----------|-----------------|----------------------|-------------------|-------------------|-------------------|-------------------|
| 0 | 0 | -2000.0 | -75000.0 | 0.0 | 0.0 | 0.0 | 0.0 |
| 1 | 6.0 | -87.0 | -50000.0 | 0.0 | 1000.0 | 0.0 | 1000.0 |
| 2 | 12.0 | -70.0 | -25000.0 | 0.0 | 500.0 | 0.0 | 500.0 |
| 3 | 18.0 | -17.0 | -5000.0 | 0.0 | 500.0 | 0.0 | 500.0 |
| 4 | 24.0 | 0.0 | -1000.0 | 0.0 | 30.0 | 0.0 | 30.0 |
| 5 | 28.0 | 0.0 | -600.0 | 0.0 | 18.0 | 0.0 | 18.0 |
| 6 | 32.0 | 0.0 | -200.0 | 0.0 | 6.0 | 0.0 | 6.0 |
| 7 | 36.0 | 0.0 | -100.0 | 0.0 | 3.0 | 0.0 | 3.0 |
| 8 | 38.0 | 0.0 | -50.0 | 0.0 | 1.5 | 0.0 | 1.5 |
| 9 | 39.0 | -0.5 | -8.0 | 0.0 | 0.15 | 0.0 | 0.15 |
| 10 | 39.75 | 0.0 | -5.0 | 0.0 | -3.0 | 0.0 | -3.0 |
| 11 | 40.5 | 0.0 | -5.0 | 0.0 | 3.0 | 0.0 | -3.0 |
| 12 | 41.25 | 0.5 | -8.0 | 0.0 | 0.15 | 0.0 | 0.15 |

servicer via inter-satellite link, and it is assumed that both satellites' attitudes are tightly controlled to ensure the crosslink antennas are always aligned.

As indicated in Table 9, navigation and control algorithms for each experiment are selected based on the mission profile. Experiments 2 through 4 use the Koenig-D'Amico control solver as the

Table 9: Specifications for each experiment in this work.

| Experiment | 1 | 2 | 3 | 4 |
|--------------------------------|---|---|---------------------------------------|--|
| Range | Far | Close | Far & Close | Far & Close |
| Waypoints (Table 8) | 0-8 | 9-12 | 0-12 | 0-12 |
| Cooperative Target? | No | No | Yes | No |
| Servicer Attitude | Camera boresight pointed at target center | Camera boresight pointed at target center | Zenith pointing | Camera boresight pointed at target center |
| Target Attitude | Tumbling | Tumbling | Zenith pointing | Tumbling |
| Navigation Algorithm(s) | AOT + SEDF | SPN + SEDF | CDGNSS + IAR + SEDF | AOT + SEDF (far-range) SPN + SEDF (close-range) |
| Control Algorithm(s) | Closed-Form | Koenig-D'Amico Least Squares (Backup) | Koenig-D'Amico Least Squares (Backup) | Koenig-D'Amico Least Squares (Backup) |
| SIL Sensor Model | OpenGL renderer | OpenGL renderer | GNSS Emulator | OpenGL renderer |
| HIL Testbed | OS | TRON | GRAND | - |
| Measurement Rate (Hz) | 0.0167 | 0.2 | 0.1 to 1 | 0.0167 (far-range) 0.2 (close-range) |

default. However, if the convex optimizer does not converge to a solution, the Least Squares solver is used as the back-up. A special case is Experiment 4, which traverses the entire reference trajectory. In this experiment, the GNC stack initially employs AOT for far-range navigation. Then, when the target's predicted size in the image exceeds a threshold of 100 pixels, the GNC stack switches to using SPN to estimate the target's relative state. The SEDF continues to run after the transition, expanding its state estimate to include relative attitude and angular rate states once SPN is active.

Experiments 1 and 2 are conducted twice, once with the SIL testing mode and once with the HIL testbeds. Experiments 3 and 4 are only run as a SIL test.

RESULTS

The results for navigation and control errors from both SIL and HIL will be shown in this section. The chosen comparison metrics are RTN navigation error and RTN control error at each waypoint time. Navigation error is the difference between the estimated and the ground truth RTN state of the target, while control error represents the deviation from the ground-truth and commanded waypoints in RTN space. These are presented as 2-norm values of the position components, since velocity errors are not applicable to the discrete testing methodology.

The calibration accuracies of each testbed are compared to statistics of navigation error, which are computed over the experiment duration. As SIL provides a performance benchmark, the RTN position error norms from SIL tests are considered the maximum allowable navigation error in each of the testbeds. This allows isolating the error introduced by the GNC stack from the error inherited from the testbed. For instance in TRON, any excess rotation and translation error in the achieved

poses will degrade the navigation estimate when using SPN. The errors from the physical testbeds are minimized through rigorous calibration processes, and are expected to be negligible compared to the errors from the GNC algorithms, to isolate the navigation errors and attribute them solely to the GNC stack.

(1) Far-Range Experiment Results

The far-range results are summarized in Table 10, where SIL corresponds to OpenGL-rendered images and HIL corresponds to images taken by the PointGrey camera from the OS testbed. For angles-only navigation, $a\delta\lambda$ is characterized by weak observability. As expected, it is the largest contributor to relative navigation error on the order of kilometers. Figure 7 reflects the divergence in $a\delta\lambda$ for both SIL and HIL.

Table 10: Far-range Experiment Metrics (AOT). Navigation and control error are expressed as L2 norms at each waypoint time.

| | Waypoint | 1 | 2 | 3 | 4 | 5 | 6 | 7 | 8 |
|-----------------------------|----------|-------|-------|--------|--------|--------|--------|--------|--------|
| RTN Position | SIL | 45.1 | 476.5 | 1306.4 | 1795.8 | 2387.0 | 2607.5 | 3161.0 | 3407.5 |
| Navigation Error (m) | HIL | 184.2 | 896.4 | 2313.6 | 3778.9 | 5070.4 | 5979.9 | 7233.7 | 7815.9 |
| RTN Position | SIL | 201.5 | 480.8 | 1175.9 | 2629.9 | 3402.4 | 3788.9 | 4774.2 | 3319.9 |
| Control Error (m) | HIL | 203.1 | 911.2 | 2380.8 | 4132.0 | 5183.0 | 5840.3 | 7103.4 | 7629.8 |

The errors in $a\delta\lambda$ are significantly more pronounced in HIL, when a physical camera was used to take images. Because all other variables are controlled in this experiment, it demonstrates a clear gap between the digital twin’s camera model and the intrinsics of real hardware. In SIL, the scene is rendered to a simplified model of the given camera’s intrinsics. But in HIL testing, the physical camera has imperfections that deviate from the digital twin and lead to more measurement errors.

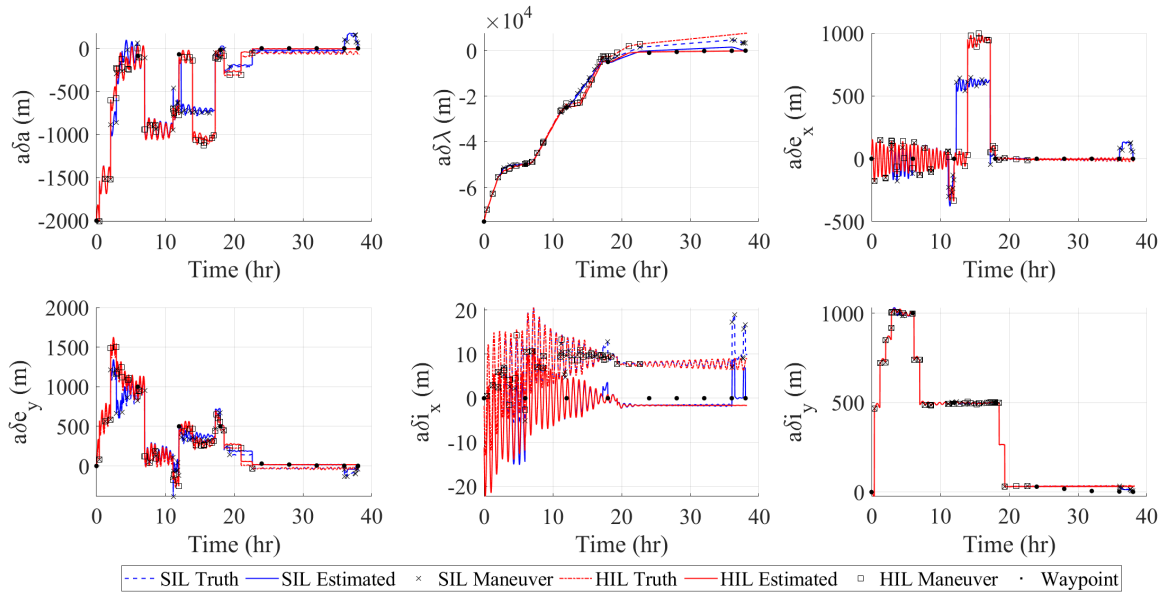


Figure 7: Results of Experiment (1): Actual, estimated, and desired ROEs of the target from SIL and HIL testing. ROEs are plotted as osculating quantities with impulsive maneuvers plotted on top.

In other ROEs such as $a\delta e_y$ and $a\delta i_y$, there is a clear correspondence between SIL and HIL testing. Both tests even show the same 10-meter bias in $a\delta i_x$. The bias is from the GNC stack

coupled with the RPO trajectory, which has little variation in the target’s out-of-plane motion in comparison to the inter-satellite distance. There are some discrepancies in $a\delta a$ and $a\delta e_x$, but these are due to large maneuvers in the radial direction before and after waypoint #2.

Figure 8 compares the cumulative Δv profile of SIL and HIL for this experiment. The greater Δv usage in SIL over HIL is tied to the relative navigation errors discussed previously. The controller’s performance boils down to the accuracy level of the navigation system. Because the target state estimate was more accurate during SIL, the GNC stack was able to execute more maneuvers that reduce control error.

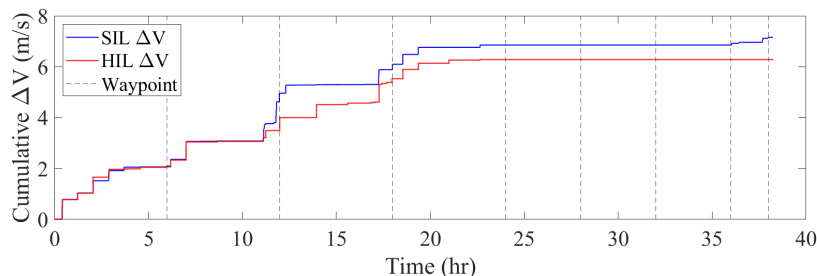


Figure 8: SIL and HIL cumulative Δv during far-range using AOT. In total, SIL executed 49 maneuvers (7.15 m/s) and HIL executed 41 maneuvers (6.28 m/s).

The results of this experiment highlight the importance of HIL due to mismatches between the digital twin and the real world. Meaningful conclusions can still be drawn from running cheap, fast SIL simulations to inform algorithm design, but SIL will greatly overpredict the performance of the navigation system.

(2) Close-Range Experiment Results

The close-range experiment results comparing SIL and HIL are given in Table 11. Similar to the far-range case, SIL yields smaller navigation errors than HIL on average. Figure 9 shows that the hardware is well represented by its digital twin, and conclusions for fast iteration on a variety of GNC algorithms may be drawn from software-only simulation.

Table 11: Close-range Experiment Metrics (SPN). L2 norms of RTN position error for navigation and control are given at each waypoint time. Statistics are computed over the experiment duration.

| | Waypoint | 10 | 11 | 12 | Mean \pm Std |
|------------------------------|----------|-------|-------|-------|-----------------|
| RTN Position | SIL | 135.8 | 82.4 | 125.7 | 90.7 ± 68.9 |
| Navigation Error (mm) | HIL | 101.4 | 190.1 | 262.2 | |
| RTN Position | SIL | 219.9 | 52.7 | 119.4 | |
| Control Error (mm) | HIL | 271.5 | 42.1 | 280.0 | |

Notice that the statistics of navigation error are much larger in comparison to the TRON calibration residuals listed in Table 4. Even when the residuals are scaled up based on the satellite mockup model, the achieved calibration accuracy is one order of magnitude lower than the mean error seen during SIL. Thus, any additional errors in HIL are strictly associated with the GNC stack.

While the time history of ROEs are very similar, SIL and HIL differ in terms of Δv cost. During HIL, the servicer executes large burns at waypoints #10 and #11 which create large spikes in $a\delta\lambda$.

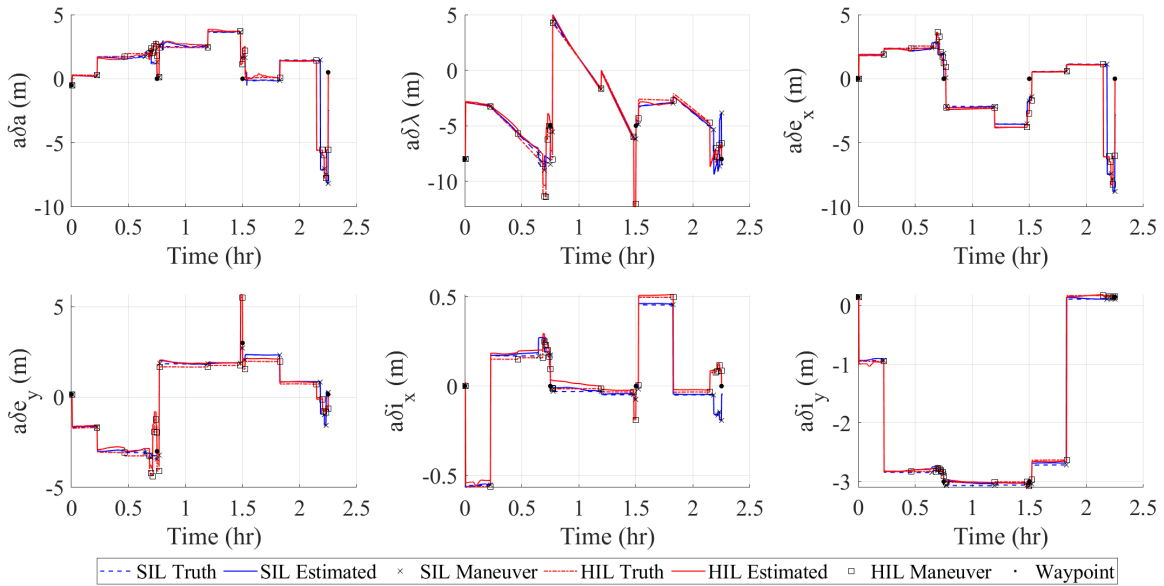


Figure 9: Close-range SIL using SPN only. Actual, estimated, and desired ROEs of the target. ROEs plotted are osculating quantities.

The target and servicer are at the closest distance, causing Tango to go partially out of frame with harsh shadows. This makes it difficult the GNC stack to plan its maneuver and react efficiently. However, these spikes do not occur in SIL under less severe lighting conditions, where SPN maintains a better state estimate.

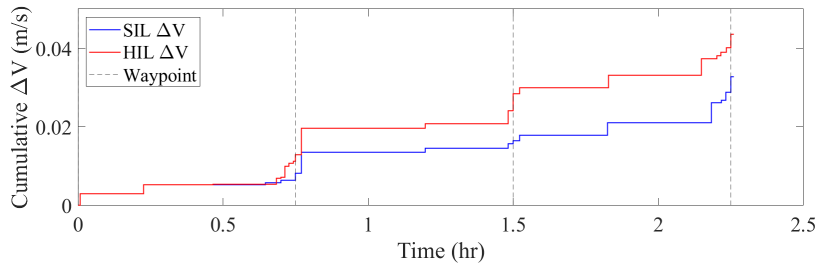


Figure 10: Cumulative ΔV during close-range using SPN only. The GNC stack executes 16 maneuvers during SIL (32.8 mm/s), and 21 maneuvers during HIL (43.5 mm/s).

This experiment demonstrates that SIL and HIL can be comparable in close-range scenarios with some tradeoffs. Although the TRON facility accurately recreates the space environment, it comes with the drawback of extended test campaigns and strict calibration requirements to eliminate sources of error. This makes SIL a viable alternative, but at the risk of underallocating Δv budget and overpredicting navigation accuracy. Ultimately, HIL testing gives more confidence in the SIL results and lends credibility to OpenGL-based renderer.

(3) Cooperative Full-Range Results

The results from the cooperative close-range experiment are shown in Figure 11 for SIL. As expected, CDGNSS with successful IAR achieves sub-centimeter navigation accuracy.

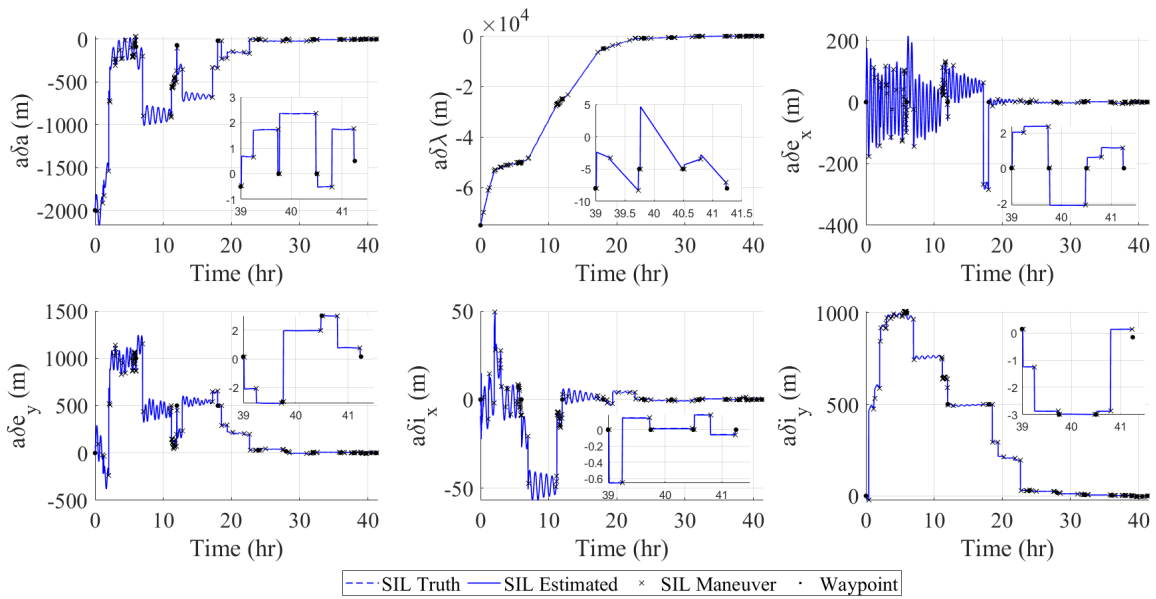


Figure 11: Full-range SIL using CDGNSS with IAR only. Zoomed in plots show close range segment beginning at 39 hours. ROEs plotted are osculating quantities. Total Δv is 4.144 m/s.

(4) Noncooperative Full-Range Results

The estimated and achieved ROEs of the SIL noncooperative full-range experiment are shown in Figure 12. This experiment is meant to demonstrate the modularity of the SIL framework, which allows multiple navigation algorithms to work in tandem (AOT and SPN).

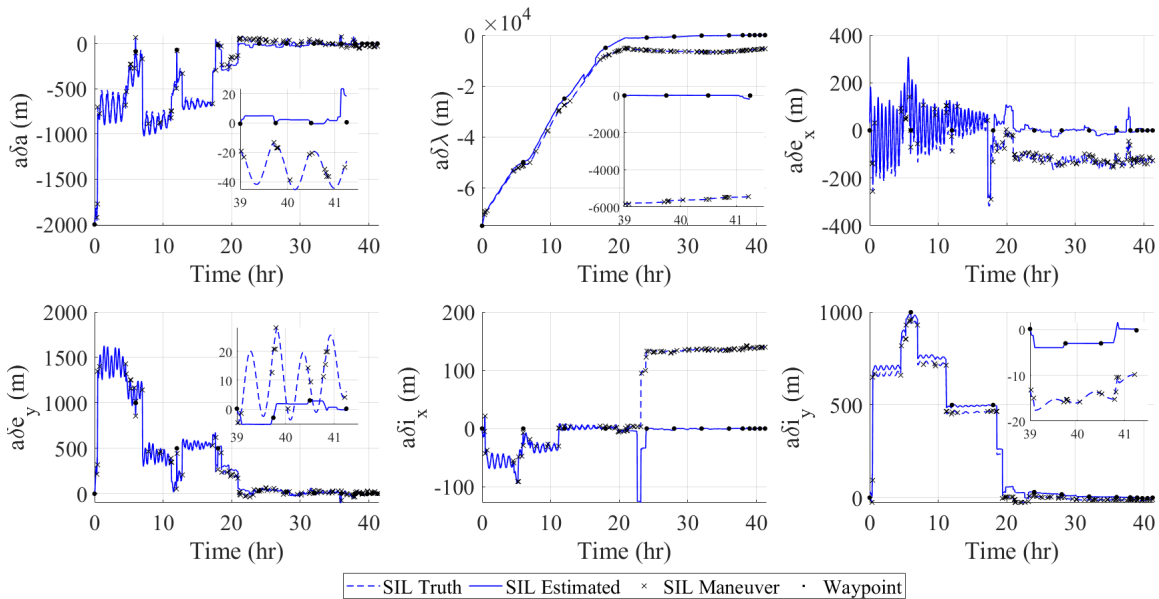


Figure 12: Full-range SIL using AOT and SPN. Zoomed in plots show close range segment beginning at 39 hours. ROEs plotted are osculating quantities. Total Δv is 6.057 m/s.

CONCLUSION

This work presents an integrated, hybrid digital and robotic twinning framework for end-to-end verification and validation (V&V) of autonomous GNC stacks for Rendezvous, Proximity Operations (RPO) and Formation Flying (FF) applications. The framework combines Software-in-the-Loop (SIL) and Hardware-in-the-Loop (HIL) methodologies to evaluate the performance of the GNC stack under real-world conditions. By incorporating three testbeds at Stanford’s Space Rendezvous Lab (SLAB), the proposed pipeline supports closed-loop testing across full mission scenarios with real spacecraft hardware. The architecture enables validation of multi-modal sensing (vision- and RF-based) and control strategies, accommodates cooperative and uncooperative targets, and captures transitions between sensing regimes.

The framework was validated through the execution of a full-range RPO mission spanning 75 km to 2.5 m using both vision-based and RF sensing modes. The RPO mission was divided into two experiments that directly compare SIL and HIL to quantify the sim-to-world gap, and two additional experiments done only in SIL. The results help to assess the robustness of navigation algorithms to sensor imperfections and measurement noise, evaluate the fidelity of digital twins, and predict mission-relevant metrics such as cumulative Δv and control error. Ultimately, the experiments demonstrate the framework’s ability to reproduce comparable scenario realizations between SIL and HIL experiments. Overall, this modular, extensible approach advances the state-of-the-art in GNC V&V by enabling high-fidelity, scalable assessments of autonomy stacks under realistic operational conditions.

Lessons Learned While HIL is a time-consuming process, it led to valuable failure mode detections that were not found solely in SIL campaigns. A major lesson was in experiment planning. Given the GNC stack’s modularity, it was important to isolate single modules and assess its performance first through SIL. Then after setting a baseline, other software and hardware elements could be incorporated in steps to ensure successful integration. When problematic interactions occurred between them, it was simpler to resolve because each component had been individually benchmarked. The experiments also informed future test specifications to investigate edge cases and take into account human factors during long test campaigns. Lastly, the determinism of the simulation environment was critical to the testing process, making bugs and unexpected behaviors easy to reproduce and diagnose. This in turn enabled the system designers to refine the algorithms in order to meet mission requirements.

Future work will include further validation of digital and robotic twins against space-based data, improved photometric modeling and calibration of the OpenGL-based renderer, and integration of a representative flight computer with all testbeds to serve as an OBC to host flight software under test.

ACKNOWLEDGMENTS

This work is funded by Infinite Orbits through AFWERX contract FA864924P1021. The authors would like to thank Justin Kruger and Hugo Dage for their support and insightful discussions.

REFERENCES

- [1] S. Sharma and S. D’Amico, “Pose Estimation for Non-Cooperative Rendezvous Using Neural Networks,” June 2019. arXiv:1906.09868 [cs], 10.48550/arXiv.1906.09868.
- [2] T. H. Park, J. Bosse, and S. D’Amico, “Robotic Testbed for Rendezvous and Optical Navigation: Multi-Source Calibration and Machine Learning Use Cases,” *2021 AAS/AIAA Astrodynamics Specialist Conference, Big Sky, Virtual*, August 9-11 2021.
- [3] C. Beierle, J. Sullivan, and S. D’Amico, “Design and Utilization of the Stanford Vision-Based Navigation Testbed for Spacecraft Rendezvous,” *Proceedings of the 9th International Workshop on Satellite Constellations and Formation Flying, University of Colorado*, 2017.
- [4] C. R. Beierle, *High fidelity validation of vision-based sensors and algorithms for spaceborne navigation*. PhD thesis, Stanford University, 2019.
- [5] V. Giraldo and S. D’Amico, “Development of the Stanford GNSS navigation testbed for distributed space systems,” *Proceedings of the 2018 International Technical Meeting of the Institute of Navigation*, 2018, pp. 837–856.
- [6] S. P. Hughes, “General mission analysis tool (gmat),” tech. rep., NASA Goddard Space Flight Center, 2016.
- [7] P. W. Kenneally, S. Piggott, and H. Schaub, “Basilisk: A Flexible, Scalable and Modular Astrodynamics Simulation Framework,” *Journal of Aerospace Information Systems*, Vol. 17, Sept. 2020, pp. 496–507. Publisher: American Institute of Aeronautics and Astronautics (AIAA), 10.2514/1.i010762.
- [8] T. M. Inc., “Aerospace Toolbox version: 24.2 (R2024b),” 2024.
- [9] M. Cols-Margenet, H. Schaub, and S. Piggott, “Modular Attitude Guidance Development using the Basilisk Software Framework,” *AIAA SPACE 2016*, Long Beach, California, American Institute of Aeronautics and Astronautics, Sept. 2016, 10.2514/6.2016-5538.
- [10] T. Bell and S. D’Amico, “Event-Driven Simulation for Rapid Iterative Development of Distributed Space Flight Software,” 2025.
- [11] T. Guffanti, T. Bell, S. Y. Low, M. Murray-Cooper, and S. D’Amico, “Autonomous guidance navigation and control of the visors formation-flying mission,” *arXiv preprint arXiv:2309.16698*, 2023.
- [12] J. J. Kruger, T. Guffanti, T. H. Park, M. Murray-Cooper, S. Y. Low, T. Bell, S. D’Amico, C. W. Roscoe, and J. Westphal, “Adaptive End-to-End Architecture for Autonomous Spacecraft Navigation and Control During Rendezvous and Proximity Operations,” *AIAA SciTech Forum*, 2024, 10.2514/6.2024-0430.
- [13] M. Wilde, C. Clark, and M. Romano, “Historical survey of kinematic and dynamic spacecraft simulators for laboratory experimentation of on-orbit proximity maneuvers,” *Progress in Aerospace Sciences*, Vol. 110, Oct. 2019, p. 100552, 10.1016/j.paerosci.2019.100552.
- [14] J. Leitner, “A hardware-in-the-loop testbed for spacecraft formation flying applications,” *2001 IEEE aerospace conference proceedings (Cat. No. 01TH8542)*, Vol. 2, IEEE, 2001, pp. 2–615.
- [15] R. Burns, B. Naasz, D. Gaylor, and J. Higinbotham, “An environment for hardware-in-the-loop formation navigation and control,” *AIAA/AAS astrodynamics specialist conference and exhibit*, 2004, p. 4735.
- [16] G. Gaias, J.-S. Ardaens, and S. D’Amico, “Formation flying testbed at dlr’s german space operations center (gsoc),” 2012.
- [17] J. Ardaens and S. D’Amico, “Formation flying testbed,” *DLR-GSOC TN*, 2009, pp. 09–01.
- [18] N. Fedora, C. Ford, and P. Boulton, “A Versatile Solution for Testing GPS/Inertial Navigation Systems,” *Proceedings of the 21st International Technical Meeting of the Satellite Division of The Institute of Navigation (ION GNSS 2008)*, 2008, pp. 1227–1236.
- [19] G. Heinrichs, M. Irsigler, R. Wolf, J. Winkel, and G. Prokoph, “NavX (R)-NCS-The First Galileo/GPS Full RF Navigation Constellation Simulator,” *Proceedings of the 20th International Technical Meeting of the Satellite Division of The Institute of Navigation (ION GNSS 2007)*, 2007, pp. 1323–1328.
- [20] S. Biswas, L. Qiao, and A. Dempster, “Space-borne GNSS based orbit determination using a SPIRENT GNSS simulator,” *15th Australian Space Research Conference, Adelaide, Australia*, 2014.
- [21] Y. Peng, *GNSS-based Spacecraft Formation Flying Simulation and Ionospheric Remote Sensing Applications*. PhD thesis, Virginia Tech, 2017.
- [22] V. Giraldo, D. Eddy, and S. D’Amico, “Development and verification of the stanford GNSS navigation testbed for spacecraft formation flying,” *Technical Note TN2017*, Vol. 1, 2017.
- [23] B. Boone, J. Bruzzi, W. Dellinger, B. Kluga, and K. Strobehn, “Optical simulator and testbed for spacecraft star tracker development,” *Optical Modeling and Performance Predictions II*, Vol. 5867, SPIE, 2005, pp. 318–331.
- [24] M. A. Samaan, S. R. Steffes, and S. Theil, “Star tracker real-time hardware in the loop testing using optical star simulator,” *Spaceflight Mechanics*, Vol. 140, 2011.

- [25] D. Roessler, D. A. Pedersen, M. Benn, and J. L. Jørgensen, "Optical stimulator for vision-based sensors," *Advanced Optical Technologies*, Vol. 3, Apr. 2014, pp. 199–207, 10.1515/aot-2013-0045.
- [26] G. Rufino, D. Accardo, M. Grassi, G. Fasano, A. Renga, and U. Tancredi, "Real-Time Hardware-in-the-Loop Tests of Star Tracker Algorithms," *International Journal of Aerospace Engineering*, Vol. 2013, No. 1, 2013, p. 505720. eprint: <https://onlinelibrary.wiley.com/doi/pdf/10.1155/2013/505720>, 10.1155/2013/505720.
- [27] T. Boge, H. Benninghoff, M. Zebenay, and F. Rems, "Using robots for advanced rendezvous and docking simulation," 2012.
- [28] T. Boge and E. Schreutelkamp, "A NEW COMMANDING AND CONTROL ENVIRONMENT FOR RENDEZVOUS AND DOCKING SIMULATIONS AT THE EPOS-FACILITY," 2002.
- [29] C. Mietner, "European Proximity Operations Simulator 2.0 (EPOS) - A Robotic-Based Rendezvous and Docking Simulator," *Journal of Large-Scale Research Facilities JLSRF*, Vol. 3, Apr. 2017, 10.17815/jlsrf-3-155.
- [30] Z. Milenkovic and C. D'Souza, "The Space Operations Simulation Center (SOSC) and closed-loop hardware testing for Orion rendezvous system design," *AIAA Guidance, Navigation, and Control Conference*, 2012, p. 5034.
- [31] H. Krüger and S. Theil, "TRON - Hardware-in-the-Loop Test Facility for Lunar Descent and Landing Optical Navigation," *IFAC Proceedings Volumes*, Vol. 43, Jan. 2010, pp. 265–270, 10.3182/20100906-5-JP-2022.00046.
- [32] J. D. Mitchell, S. P. Cryan, D. Strack, L. L. Brewster, M. J. Williamson, R. T. Howard, and A. S. Johnston, "Automated Rendezvous and Docking Sensor Testing at the Flight Robotics Laboratory," *2007 IEEE Aerospace Conference*, Mar. 2007, pp. 1–16. Journal Abbreviation: 2007 IEEE Aerospace Conference, 10.1109/AERO.2007.352723.
- [33] S. Kwok Choon, M. Wilde, C. Saffom, and M. Romano, "Kinematic and Dynamic Spacecraft Maneuver Simulators for Verification and Validation of Space Robotic Systems," 08 2020, 10.2514/6.2020-1919.
- [34] D. C. Sternberg, C. Pong, N. Filipe, S. Mohan, S. Johnson, and L. Jones-Wilson, "Jet Propulsion Laboratory small satellite dynamics testbed simulation: On-orbit performance model validation," *Journal of Spacecraft and Rockets*, Vol. 55, No. 2, 2018, pp. 322–334.
- [35] J. D. Wapman, D. C. Sternberg, K. Lo, M. Wang, L. Jones-Wilson, and S. Mohan, "Jet Propulsion Laboratory Small Satellite Dynamics Testbed Planar Air-Bearing Propulsion System Characterization," *Journal of Spacecraft and Rockets*, Vol. 58, No. 4, 2021, pp. 954–971, 10.2514/1.A34857.
- [36] J. A. Tappe, *Development of Star Tracker System for Accurate Estimation of Spacecraft Attitude*. PhD thesis, Naval Postgraduate School, 2009.
- [37] M. Mote, M. Egerstedt, E. Feron, A. Bylard, and M. Pavone, "Collision-Inclusive Trajectory Optimization for Free-Flying Spacecraft," *Journal of Guidance, Control, and Dynamics*, Mar. 2020. Publisher: American Institute of Aeronautics and Astronautics, 10.2514/1.G004788.
- [38] P. Tsiotras, "ASTROS: A 5DOF experimental facility for research in space proximity operations," *Advances in the Astronautical Sciences*, Vol. 151, 01 2014, pp. 717–730.
- [39] Y. Nakka, R. Foust, E. Lupu, D. Elliott, I. Crowell, S.-J. Chung, and F. Hadaegh, *Six Degree-of-Freedom Spacecraft Dynamics Simulator for Formation Control Research*. AIAA, Aug. 2018.
- [40] J. R. Dormand and P. J. Prince, "A family of embedded Runge-Kutta formulae," *Journal of Computational and Applied Mathematics*, Vol. 6, Mar. 1980, pp. 19–26, 10.1016/0771-050X(80)90013-3.
- [41] J. M. Picone, A. E. Hedin, D. P. Drob, and A. C. Aikin, "NRLMSISE-00 empirical model of the atmosphere: Statistical comparisons and scientific issues," *Journal of Geophysical Research: Space Physics*, Vol. 107, No. A12, 2002, pp. S15–1–S15–16. eprint: <https://agupubs.onlinelibrary.wiley.com/doi/pdf/10.1029/2002JA009430>, 10.1029/2002JA009430.
- [42] Novatel, "OEM7 Commands and Logs Reference Manual," 2025.
- [43] S. Y. Low, T. Bell, and S. D'Amico, "Flight-Ready Precise and Robust Carrier-Phase GNSS Navigation Software for Distributed Space Systems," *AIAA Scitech 2026 Forum (In-Review)*, 2026.
- [44] M. L. Psiaki and S. Mohiuddin, "Modeling, analysis, and simulation of GPS carrier phase for spacecraft relative navigation," *Journal of Guidance, Control, and Dynamics*, Vol. 30, No. 6, 2007, pp. 1628–1639.
- [45] C. Beierle and S. D'Amico, "Variable-magnification optical stimulator for training and validation of spaceborne vision-based navigation," *Journal of Spacecraft and Rockets*, Vol. 56, No. 4, 2019, pp. 1060–1072.
- [46] *Leica AT403 User Manual*, 1.1 ed., 2020.
- [47] P. Teunissen, "A new method for fast carrier phase ambiguity estimation," *Proceedings of 1994 IEEE Position, Location and Navigation Symposium-PLANS'94*, IEEE, 1994, pp. 562–573.

- [48] S. Y. Low and S. D'Amico, "Precise distributed satellite navigation: Differential GPS with sensor-coupling for integer ambiguity resolution," *2024 IEEE Aerospace Conference*, IEEE, 2024, pp. 1–18.
- [49] J. Kruger and S. D'Amico, "Autonomous angles-only multitarget tracking for spacecraft swarms," *Acta Astronautica*, Vol. 189, 2021, pp. 514–529.
- [50] T. H. Park and S. D'Amico, "Robust multi-task learning and online refinement for spacecraft pose estimation across domain gap," *Advances in Space Research*, Mar. 2023, 10.1016/j.asr.2023.03.036.
- [51] V. Giraldo and S. D'Amico, "Distributed multi-GNSS timing and localization for nanosatellites," *NAVIGATION*, Vol. 66, No. 4, 2019, pp. 729–746. eprint: <https://onlinelibrary.wiley.com/doi/pdf/10.1002/navi.337>, 10.1002/navi.337.
- [52] J. Sullivan, A. W. Koenig, J. Kruger, and S. D'Amico, "Generalized Angles-Only Navigation Architecture for Autonomous Distributed Space Systems," *Journal of Guidance, Control, and Dynamics*, Vol. 44, June 2021, pp. 1087–1105. Publisher: American Institute of Aeronautics and Astronautics, 10.2514/1.G005439.
- [53] T. H. Park and S. D'Amico, "Adaptive Neural-Network-Based Unscented Kalman Filter for Robust Pose Tracking of Noncooperative Spacecraft," *Journal of Guidance, Control, and Dynamics*, Vol. 46, Sept. 2023, pp. 1671–1688, 10.2514/1.G007387.
- [54] X. W. Chang, X. Yang, and T. Zhou, "MLAMBDA: A modified LAMBDA method for integer least-squares estimation," *Journal of Geodesy*, Vol. 79, 2005, pp. 552–565.
- [55] M. Chernick and S. D'Amico, "Closed-Form Optimal Impulsive Control of Spacecraft Formations Using Reachable Set Theory," *Journal of Guidance, Control, and Dynamics*, Vol. 44, Jan. 2021, pp. 25–44. Publisher: American Institute of Aeronautics and Astronautics, 10.2514/1.G005218.
- [56] M. Chernick and S. D'Amico, "New Closed-Form Solutions for Optimal Impulsive Control of Spacecraft Relative Motion," *Journal of Guidance, Control, and Dynamics*, Vol. 41, Feb. 2018, pp. 301–319. Publisher: American Institute of Aeronautics and Astronautics, 10.2514/1.G002848.
- [57] A. W. Koenig and S. D'Amico, "Fast algorithm for fuel-optimal impulsive control of linear systems with time-varying cost," *IEEE Transactions on Automatic Control*, Vol. 66, No. 9, 2020, pp. 4029–4042.
- [58] S. D'Amico, J.-S. Ardaens, G. Gaias, H. Benninghoff, B. Schlepp, and J. L. Jørgensen, "Noncooperative Rendezvous Using Angles-Only Optical Navigation: System Design and Flight Results," *Journal of Guidance, Control, and Dynamics*, Vol. 36, Nov. 2013, pp. 1576–1595. Publisher: American Institute of Aeronautics and Astronautics, 10.2514/1.59236.
- [59] S. D'Amico, *Autonomous formation flying in low earth orbit*. PhD thesis, TU Delft, 2010.